Nanoscale

PAPER

View Article Online
View Journal | View Issue

Cite this: *Nanoscale*, 2025, **17**, 11366

Tuning the nanoscale tribological characteristics of thermally evaporated transparent polyaniline–graphene nanocomposite thin films†

Soumyasuravi Thakur, ‡[a] Debottam Datta, ‡[b] Jitendra P. Singh, [b,c] Nitya N. Gosvami *[a,b] and Nirat Ray *[a]

Received 30th December 2024,
Accepted 20th March 2025

DOI: 10.1039/d4nr05482b

rsc.li/nanoscale

In this work, we report the development of a solvent-free technique to fabricate optically transparent polyaniline (PANI)–graphene thin films with precise control over both composition and thickness. By systematically varying the PANI–graphene composition, we investigate the influence of graphene reinforcement on the mechanical and tribological properties of the polymer films. A comprehensive suite of surface characterization techniques, combined with atomic force microscopy (AFM) based nanotribological testing, reveals how embedded graphene patches act as lubricating agents within the polymer matrix. More specifically, the study shows how the friction force and the coefficient of friction (COF) vary on the surface of the polyaniline–graphene composite film with the variation of graphene percentage. These findings provide crucial insights into the interfacial behavior of PANI–graphene nanocomposites and highlight the potential of such materials for next-generation applications where tailored frictional and mechanical performance is essential. This study bridges the gap between material design and practical performance, contributing to the advancement of nanocomposite thin film technologies for diverse applications.

Introduction

The pursuit of advanced materials with tailored physical and chemical properties has driven significant research into the development of nanocomposites,[1] where integrating nanomaterials into a polymer matrix can yield enhanced performance characteristics. Among these, polymer–graphene nanocomposites represent a fascinating frontier due to their exceptional mechanical,[2] electrical,[3] and thermal properties.[4] Graphene, a single layer of carbon atoms arranged in a hexagonal lattice, has garnered considerable attention for its remarkable strength,[5] high thermal conductivity,[6] and excellent electrical properties.[7] Graphene is also an excellent solid lubricant, and even a monolayer thick graphene coating can provide superlubric surface coatings with extremely high wear resistance.[8] When incorporated into polymer matrices, graphene can substantially alter the surface morphology and tribological behavior of the resulting nanocomposite films. Polyaniline (PANI) is recognized as a valuable conducting polymer,[9] extensively used in electronic, optical, and electrochemical applications, because of its good environmental stability,[10] low cost, interesting electroactivity,[11] and uncommon doping/dedoping chemistry.[12–14] Combining the distinctive characteristics inherent to graphene and PANI leads to enhancements in properties such as electrical conductivity,[15,16] electrocatalytic activity,[17] and thermal stability.[4] Consequently, these nanocomposites find extensive utility across diverse applications, including supercapacitors,[18–20] sensing platforms,[21–23] and electrochromic devices.[24,25] PANI–graphene composites have also been explored for various tribological applications. Maurya *et al.*[26] developed PANI graphene composite-based epoxy coatings on $Mg_9Li_7Al_1Sn$ and $Mg_9Li_5Al_3Sn_1Zn$ alloys and achieved significant improvements in mechanical, tribological, and anti-corrosion properties. The coefficient of friction (COF) was reduced drastically in the PANI–graphene composite-based epoxy coatings compared to the pure epoxy coating alone. Liu *et al.*[27] added a PANI and graphene oxide (GO) composite as

[a]*Department of Materials Science and Engineering, Indian Institute of Technology Delhi, Hauz Khas, New Delhi-110016, India. E-mail: ngosvami@iitd.ac.in, nirat@iitd.ac.in*

[b]*School of Interdisciplinary Research (SIRe), Indian Institute of Technology Delhi, Hauz Khas, New Delhi-110016, India*

[c]*Department of Physics, Indian Institute of Technology Delhi, Hauz Khas, New Delhi-110016, India*

†Electronic supplementary information (ESI) available: Optical images of the thin films; UV-vis transmittance spectra of pure PANI and all nanocomposite thin films; Raman spectra, D and G band mapping; thickness measurement using surface profilometry; topography and lateral force maps along with the friction loops of 35%, 15%, and 10% graphene composite films; comparative analysis among the lateral force maps of 35%, 15%, 10%, and 5% graphene composite films; variation of lateral force maps with increasing normal loads for the 35%, 10%, and 5% graphene composite and pure PANI films. See DOI: https://doi.org/10.1039/d4nr05482b

‡These authors contributed equally to this work.

an additive to paraffin oil and performed a four-ball friction test using GCr_{15} balls. The COF significantly reduced in comparison with the pure liquid paraffin oil, paraffin oil + GO, and paraffin oil + PANI, respectively. Verma *et al.*[28] prepared additives combining yttrium (Y) and vanadium (V) doped ZnO particles, PANI, and a reduced GO composite and dispersed them in paraffin oil to achieve superlubricity and significant reduction in wear. Cao *et al.*[29] synthesized ionic liquid-doped PANI and used it as an additive in two different lubricant media (poly-alpha olefin/poly-urea grease and polyethylene glycol) to minimize the friction and wear between AISI 52100 steel pairs. Along with ionic-liquid doping PANI, Xia *et al.*[30] combined WS_2 and prepared a new additive to improve the tribological properties. They added this newly developed composite to the lithium complex grease and minimized the friction between GCr_{15} steel ball–plate pairs. Singh *et al.*[31] performed a tribological test on a four-ball tester using paraffin oil and adding PANI and vanadium pentoxide additives and achieved a significant reduction in the COF in comparison with the pure paraffin oil. Lin *et al.*[32] developed composite fiber using polyamide, carbon fiber, and polyaniline nanofiber, which exhibited reduced wear and stable friction in comparison with the polyamide–carbon fiber composite alone. In all the tribological studies, PANI and its composites are used as additives in the lubrication medium, and friction reduction is achieved due to the combined effect of the lubricating filler material and stable film formation between the two surfaces rubbing against each other. However, it has not been explored as a solid lubricant in the form of a thin coating for improving the tribological properties.

When developed as a coating, the surface morphology, encompassing the distribution, alignment, and interaction of graphene within the polymer matrix, can significantly influence properties such as surface roughness, wettability, and adhesion. Furthermore, while the incorporation of graphene into polymer matrices can modify the tribological behavior of the films, potentially leading to enhanced wear resistance and reduced friction, there is no fundamental understanding of the mechanisms governing them, primarily due to the high variability introduced through existing fabrication processes. In this work, we have developed a solvent-free technique to create thin polyaniline (PANI)–graphene nanocomposite films with varying PANI–graphene concentrations and a very high degree of control over the thickness of the films. Through a combination of surface characterization techniques and tribological testing, we seek to provide a comprehensive understanding of how graphene reinforcement influences the mechanical and frictional properties of polymer films. The controlled fabrication process allows us to control the frictional properties of the film deposited and, in turn, yields important insights into how the friction force and COF are reduced due to the lubricating effect of graphene patches embedded in the polymer matrix. By bridging the gap between material design and practical performance, this study contributes to the development of next-generation nanocomposite materials with tailored properties for a wide range of applications.

Nirat Ray

Dr Nirat Ray completed her Ph. D. from the Massachusetts Institute of Technology (MIT) in 2014. She currently serves as an Associate Professor in the Department of Materials Science and Engineering at the Indian Institute of Technology (IIT) Delhi. Her research focuses on the experimental and first-principles design of novel artificial solids constructed from nanoscale building blocks, as well as the study of electronic and quantum metamaterials. Throughout her career, Dr Ray has been honored with several prestigious awards, including the International Fulbright Science and Technology Award and the Schlumberger Foundation Faculty for the Future Fellowship.

Experimental details

Materials

Polyaniline emeraldine base (EB) and graphene (4–10% edge oxidized, procured from Sigma Aldrich) were used further without any treatment. The nanocomposites were synthesized using a solution mixing route, where graphene was dispersed in DI water and PANI was dispersed in dimethylformamide using a magnetic stirrer. These two solutions were mixed and probe-sonicated for 45 minutes to obtain a properly blended composite. The composite was then dried in a hot air oven at 80 °C, and the resultant mixture was collected and ground into a fine homogeneous powder using a mortar and pestle. The graphene composition was varied, and a series of nanocomposite materials with graphene concentrations of 0, 5, 10, 15, and 35 wt% (see Table 1 in ESI section 1†) were synthesized. The powders were used as targets for preparing the PANI–graphene nanocomposite films.

Fabrication of PANI–graphene nanocomposite films

A fixed quantity of the prepared PANI–graphene powders was placed in a quartz crucible in an effusion cell of a thermal evaporator. The distance between the substrate holder and the target was set at 17 cm, while the target holder was a quartz crucible with an inner diameter of 9 mm. A schematic of the deposition system is shown in Fig. 1(a). The deposition temperature was maintained between 300 and 380 °C, and the pressure was kept lower than 1.3×10^{-6} mbar. The filament heating rate was set at 3 °C per minute. Once the desired temperature was reached, the shutter was opened, and deposition proceeded for a specified time to achieve a continuous thin film with a deposition rate of 0.1 Å s^{-1}. Films were deposited

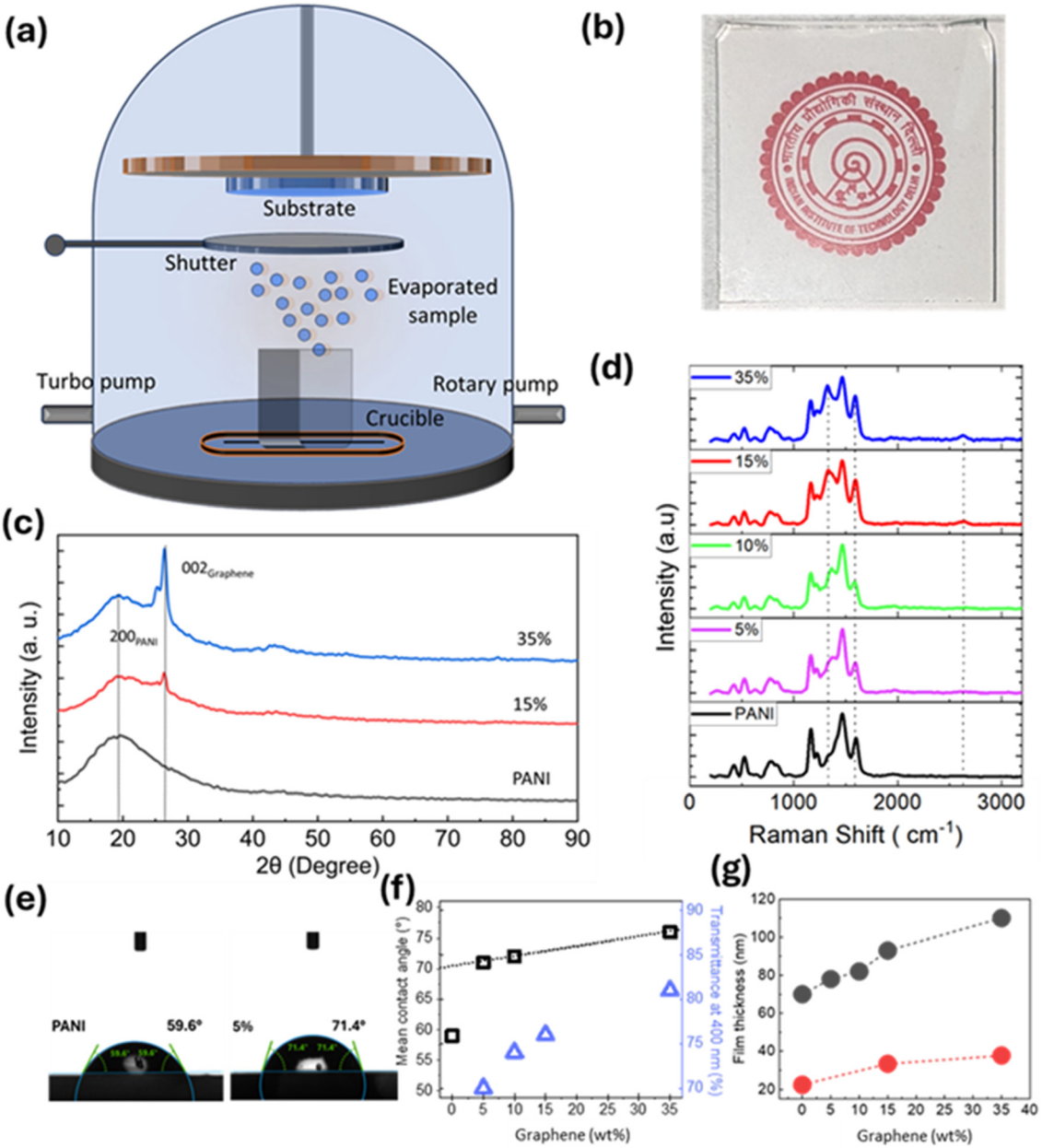

Fig. 1 (a) Schematic of the thermal evaporation process used for nanocomposite film fabrication. (b) Optical transparency of the ultrathin polymer–graphene nanocomposite film. The film is placed over a printed logo, clearly revealing the logo's details through the transparent film, demonstrating its high degree of optical clarity. (c) GIXRD diffractogram revealing emerging graphene peak intensities with increasing graphene concentrations. (d) Raman shifts for varying graphene concentrations. (e) Contact angle measurements of pure PANI (left) and the 5% graphene film. (f) Variation of the mean contact angle (black squares, left axis) and transmittance at 400 nm (blue triangles, right axis) with increasing graphene concentrations. (g) Film thickness for different graphene concentrations. Black and red spheres indicate thickness values corresponding to deposition times of 1 hour and 2 hours, respectively.

on glass slides, which were subjected to a standard Piranha cleaning solution (3 : 1 ratio of H_2SO_4/H_2O_2) and finally dried off with a nitrogen jet.

Characterization of PANI–graphene nanocomposite films

The optical transparency of the PANI–graphene nanocomposite films was subjected to inspection by the naked eye and further quantified using a UV-VIS spectrometer (Shimadzu). Detailed structural information of the thin films was examined using grazing incident angle X-ray diffraction (GIXRD, Malvern PANalytical MODEL: Empyrean). The incorporation of graphene was confirmed using a Raman spectrometer (Renishaw) at 514 nm. The contact angle measurements were obtained using a Drop Shape analyzer (KRUSS DA 25) for

examining the surface wettability of the thin polymer–graphene nanocomposite films, revealing how graphene incorporation influences the hydrophobic or hydrophilic nature of the films. Film thickness was measured using a stylus-type surface profiler (Alfa Step IQ, KLA-T).

Measurement of the friction force and coefficient of friction (COF)

The friction test on the pure PANI and PANI + graphene composite films was performed under ambient conditions using the Lateral Force Microscopy (LFM) module of a commercial atomic force microscope (AFM, FlexAFM, Nanosurf, Switzerland). The lateral force was measured using a sharp commercial AFM cantilever (ContDLC, BudgetSensors, Bulgaria), specially manufactured for the LFM and contact mode operation. The cantilever was made of silicon with a normal spring constant of 0.2 N m^{-1}. The normal spring constant of the cantilever was determined using the Sader and Green method.[33,34] The friction test was performed multiple times on the pure PANI and PANI + graphene (35%, 15%, 10% and 5%) composite thin films, selecting an area of 3 × 3 sq. μm, and simultaneously, the friction data were procured over a 256-line map with a scan rate of 20 μm s^{-1}. The friction values were quantified by dividing the difference between forward (trace) and backward (retrace) lateral signals by two to avoid the vertical offsets in the friction loops caused by the laser misalignments. The frictional errors depicted in Fig. 2(a) were quantified by calculating the standard deviation of the friction force measured in each line scan.[35] Then, the COF was calculated by measuring the slope of the friction force *vs.* normal load curve, and the error bars in Fig. 2(b) represent the slope error. The friction data were processed in batch to batch and analyzed using a customized MATLAB code. All the topography images and lateral force maps were processed using commercially available image processing software (Gwyddion), and the graphs were plotted using another commercially available scientific software, Origin.

Results and discussion

Surface morphology and physical properties of PANI–graphene nanocomposite films

The thin PANI–graphene nanocomposite films appeared transparent to the naked eye, with remarkable clarity when placed over a printed logo, as shown in Fig. 1(b). This optical transparency indicates that the films possess a high degree of uniformity and minimal optical interference, suggesting that integrating graphene into the polymer matrix does not significantly disrupt the film's optical properties. This clear visibility allowed for a detailed examination of surface morphology and provided a basis for assessing the functional performance of the films in subsequent tests. The inclusion of graphene into the thin films was first confirmed using GIXRD measurements, which show the emergence of a graphene peak with increasing concentrations of 15% and 35% respectively (see Fig. 1(c)). The intensity of the graphene peak was too low to be observed for lower concentrations of 5% and 10%. We further used Raman spectroscopy to verify the inclusion of graphene into the film, especially at lower concentrations. Enhancement of intensities of G, D, and 2D bands was observed for all non-zero graphene concentration films, confirming the inclusion of graphene into the films (see Fig. 1(d)).

The surface of the film was further analyzed through contact angle measurements, which provided insights into the wettability and surface energy characteristics of the films. The contact angle for the thin PANI film was found to be ~60°. Upon the addition of graphene, the surface properties of the nanocomposite films were significantly altered. We find that in the film with 5% graphene, the contact angle increases to ~70°, and with a subsequent increase in graphene concentration, the contact angle increases almost linearly (see Fig. 1(e and f)). This effect can be attributed to the graphene's high surface area and low surface energy, which can amplify the hydrophobic characteristics of the nanocomposite film. These changes in surface properties are crucial for tailoring the

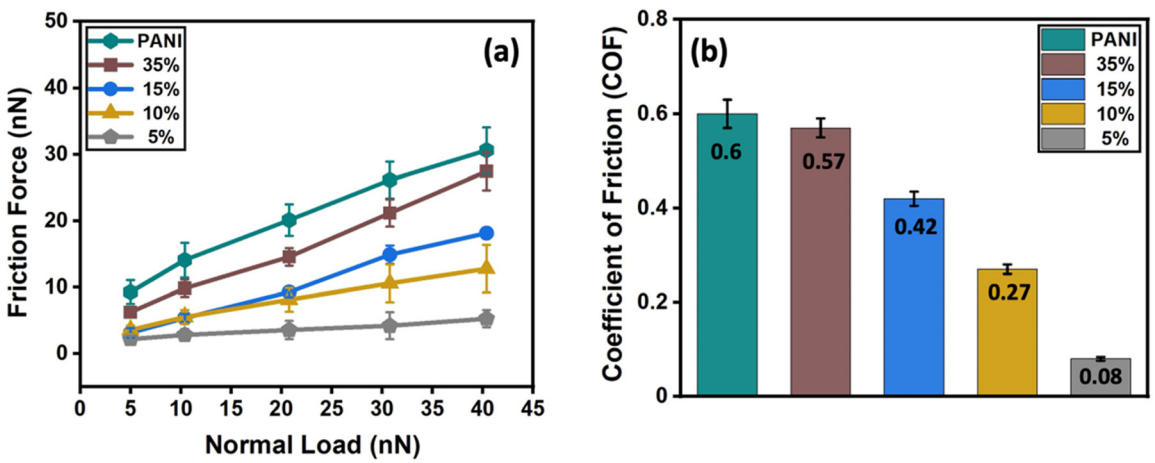

Fig. 2 (a) Variation of friction force with increasing normal loads and (b) variation of the COF with different graphene concentrations.

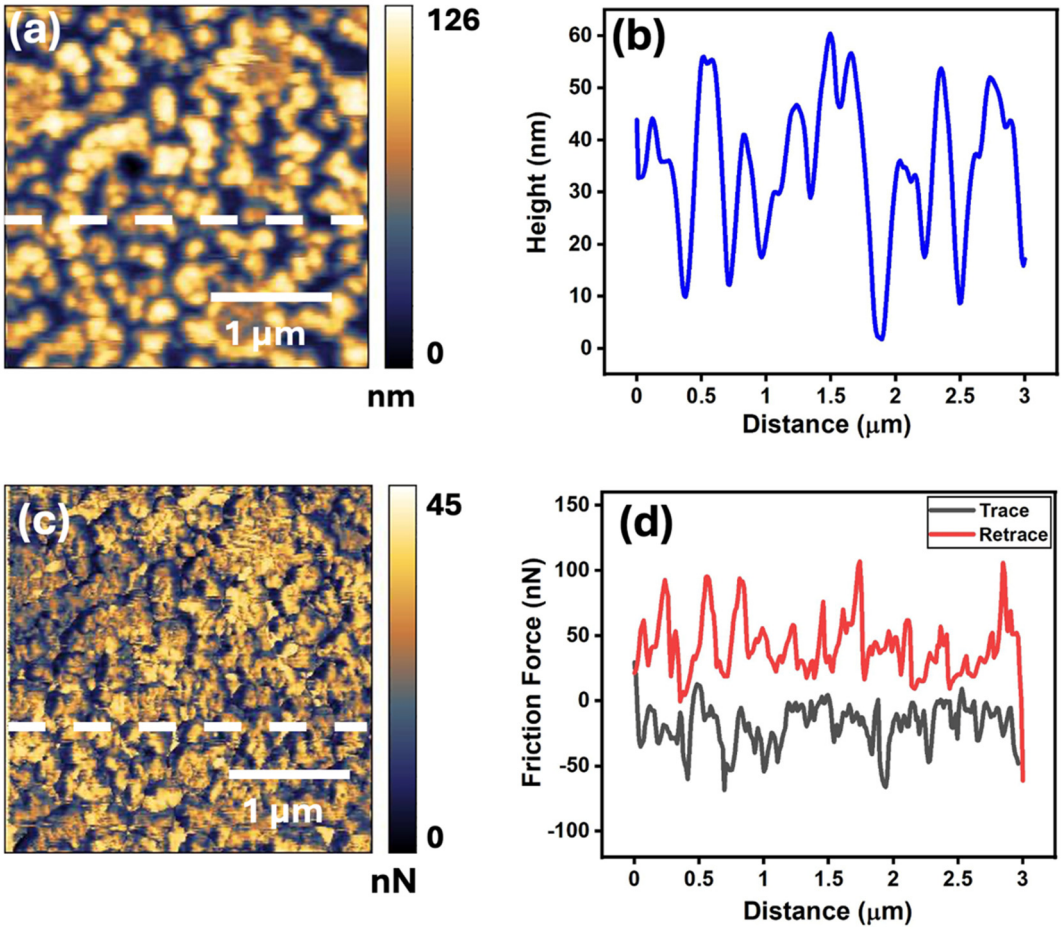

Fig. 3 LFM performed on the pure PANI thin film applying a normal load of 10 nN using a sharp AFM tip: (a) topography of the pure PANI thin film and (b) the profile of the white line from image a; corresponding (c) lateral force map (captured during the forward movement of the cantilever/trace motion) and (d) the profile of the white line or the friction loop from image c.

nanocomposite films for various applications where specific wettability characteristics are desired. The optical transmittance of the films was further characterized using a UV-VIS spectrophotometer, and once again, the transmittance was seen to increase with increasing graphene concentration (see Fig. 1(f)). A stylus-type surface profiler was used to measure the film thickness (see Fig. S3†). These measurements revealed that, for the same deposition time, the film thickness increased with higher graphene concentrations (see Fig. 1(g)).

Nanotribological properties of the PANI–graphene composite thin films

The friction of the pure PANI and the PANI–graphene nanocomposite thin films was quantified at the nanoscale level using LFM under five different normal loads, including 5 nN, 10 nN, 20 nN, 30 nN, and 40 nN, using a sharp AFM tip. After that, the COF for each separate film was determined by calculating the slope of the linear friction force *versus* the normal load curve. Fig. 2(a) and (b) show that the friction force and COF were the highest in the pure PANI thin film and were reduced in the PANI–graphene composite thin films. More interestingly, both the friction force and COF varied coherently amongst the PANI–graphene composite thin films with the change in graphene concentration. The friction force was higher in the film, which was fabricated by evaporating the PANI–graphene nanocomposite containing a 35% graphene filler (referred to as 35%), and it systematically decreased as the graphene concentration was lowered. It was seen that the COF was lowest (0.08) for 5% graphene and then subsequently increased with the increasing concentration of graphene in the composite. The pure PANI film exhibited the highest COF of 0.6, and it was slightly reduced to 0.57 in the case of the 35% graphene film. This can be easily attributed to the role of the filler material *i.e.* graphene as a solid lubricant.[36–39] Graphene is nothing but a single layer of graphite where carbon atoms are hexagonally coordinated by pseudo-two-dimensional sp^2 bonding, and two layers of graphene are bonded by weak van der Waals forces in the third dimension. Due to this unique structure, the graphene layers are more prone to delaminate or shear, and it exhibits excellent lubricating properties.[40,41] As the composite thin films had graphene fillers, they exhibited lower friction force in comparison with the pure PANI thin

film. However, the answer to the reduction in friction force and the COF with reducing graphene filler concentration is linked to the distribution of graphene on the film surface.

Fig. 3 and 4 present the topography and lateral force maps of pure PANI and 5% graphene nanocomposite thin films, respectively. In Fig. 4c, the lateral force map of the 5% graphene composite film highlights the distribution of graphene within the PANI matrix, showing reduced friction compared to the pure PANI matrix. The bright yellow patches (marked with red dotted ellipses) in this map indicate the dispersed graphene, whereas Fig. 3c confirms the absence of graphene in the pure PANI matrix. Topography and lateral force maps for PANI composites with 35%, 15%, and 10% graphene, along with their friction loops, are shown in Fig. S4, S5, and S6.† The lateral force maps reveal prominent contrasts due to graphene's effect on friction, whereas the topographic images show less pronounced differences, as they primarily depict height variations rather than frictional differences.

AFM imaging and friction measurements were conducted in a 3 × 3 μm^2 area, subdivided into 256 lines. The friction loops, shown in Fig. 4d, S4d, S5d, and S6d,† correspond to the white line profiles on the lateral force maps (Fig. 4c, S4c, S5c, and S6c†). The trace (black line) and retrace (red line) represent the forward and backward motions of the AFM cantilever, respectively, with the gap between these lines quantifying the friction force. The friction loops indicate that graphene patches (marked with blue arrows) exhibit significantly reduced friction compared to the PANI matrix (marked with green arrows). In contrast, the pure PANI matrix, shown in Fig. 3d, does not display reduced friction due to the lack of the graphene filler.

It was expected that the friction force of the pure PANI thin film would be higher than that of the PANI–graphene composite films, due to the lubricating effect of graphene. However, the opposite trend in expected variation in the friction force and COF with different graphene concentrations remains intriguing. The comparative lateral force maps, along with their friction loops, provide insights to interpret this result, which also relates to the surface morphology of the nanocomposite films. In contrast to the nomenclature of the thin films, the comparative lateral force maps showed that the percentage of dispersed graphene on the surface of the film was the highest for the 5% graphene nanocomposite film, and the proportion

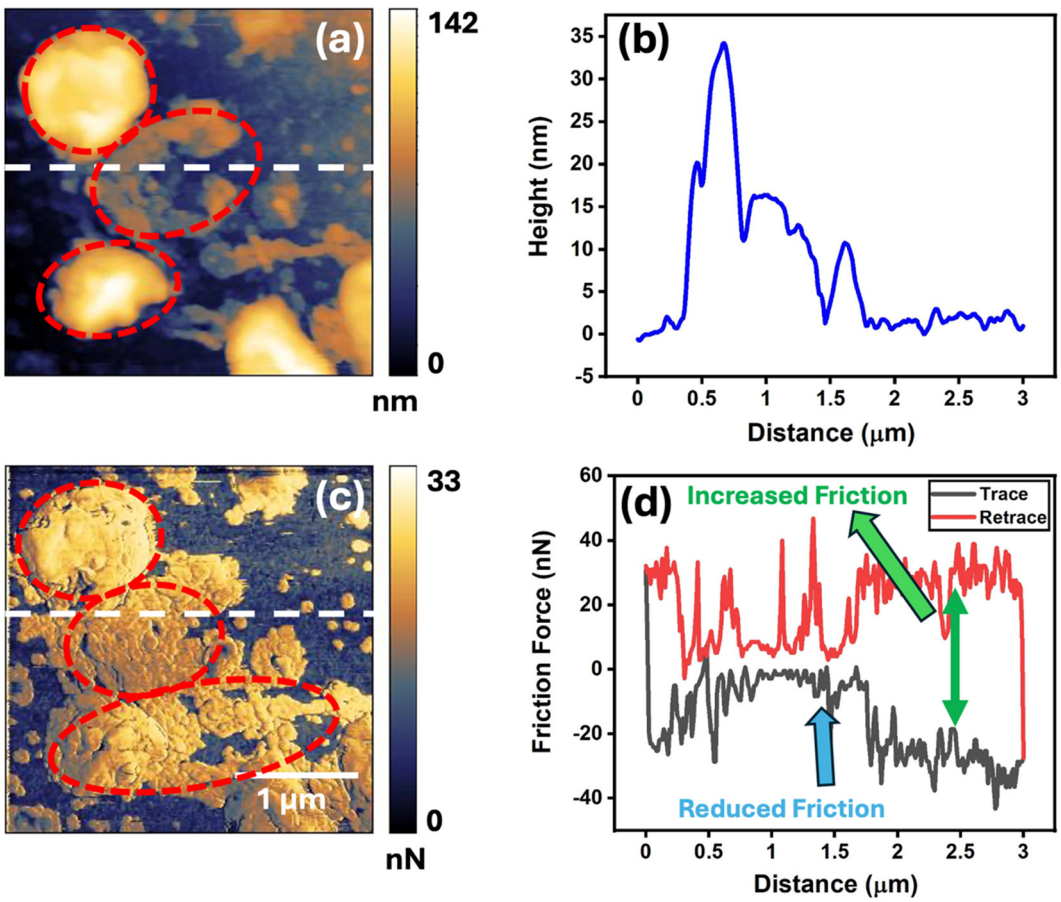

Fig. 4 LFM performed on the 5% graphene composite thin film applying a normal load of 10 nN using a sharp AFM tip: (a) topography of the thin film and (b) the profile of the white line from image a; corresponding (c) lateral force map (captured during the forward movement of the cantilever/trace motion) and (d) the profile of the white line or the friction loop from image c.

of graphene on the surface of the PANI matrix was gradually decreased in order *i.e.* 10% graphene, 15% graphene, and 35% graphene composite films, respectively (Fig. S11†). As the percentage of graphene on the surface was highest in the 5% graphene film, it exhibited the lowest friction force in comparison with the other composite films due to the higher lubrication effects of graphene, and gradually the friction increased systematically from the 5% graphene composite film to the 35% graphene composite.

The observed variation in the surface graphene content is consistent with other observations in the fabrication process. Due to graphene's high sublimation temperature, it is believed to be carried to the glass substrate by the PANI matrix during evaporation. As the nanocomposite target is thermally melted in the crucible, the graphene flakes are expected to float on the surface of the melt. At low graphene concentrations, these are carried to the substrate, and a high surface concentration results. At higher graphene concentrations, the graphene is expected to agglomerate, and therefore, a higher volume of polymer aggregation around the graphene flakes would carry them to the substrate, resulting in graphene flakes being buried in the bulk of the film. The agglomeration theory is also supported by the inability to create films beyond 35% graphene concentration, as the weight of the agglomerated flakes on the surface of the melt becomes more than what the polymer vapors can carry to the substrate. Hence, the proportion of graphene on the surface of the films was highest in the 5% graphene film and decreased with increasing graphene content in the precursor bath.

Although the friction force varied significantly with the variation of the embedded graphene filler in the PANI matrix, it is not necessary that the COF would follow the same trend. Here, the friction force depended on the applied normal load and the concentration of the embedded graphene on the PANI matrix. For each thin film, the friction was calculated separately at different normal loads from 5 nN to 40 nN, and it increased with increasing normal load. At the same time, the trend showed that the overall friction force decreased from the 35% graphene film to the 5% graphene film with increasing embedded graphene concentration in the PANI matrix. However, the COF was determined by quantifying the slope of the linear friction force *versus* the normal load curve. The COF was also found to systematically decrease in order from the pure PANI film to the 5% graphene composite thin film (Fig. 2(b)) and achieved a significantly lower value of up to 0.08. To interpret this result, the evolution of lateral force maps with increasing normal loads for each different thin film needs to be observed (see Fig. 5, S12–S14†). In Fig. 5, it is interesting to see how the embedded graphene patches of the 15% graphene composite thin film were gradually wearing out of the PANI matrix with increasing normal loads. When the applied normal load was up to 10 nN, the graphene patches were intact in the PANI matrix; however, as the load increased to 20 nN, the graphene patches started to wear out and they

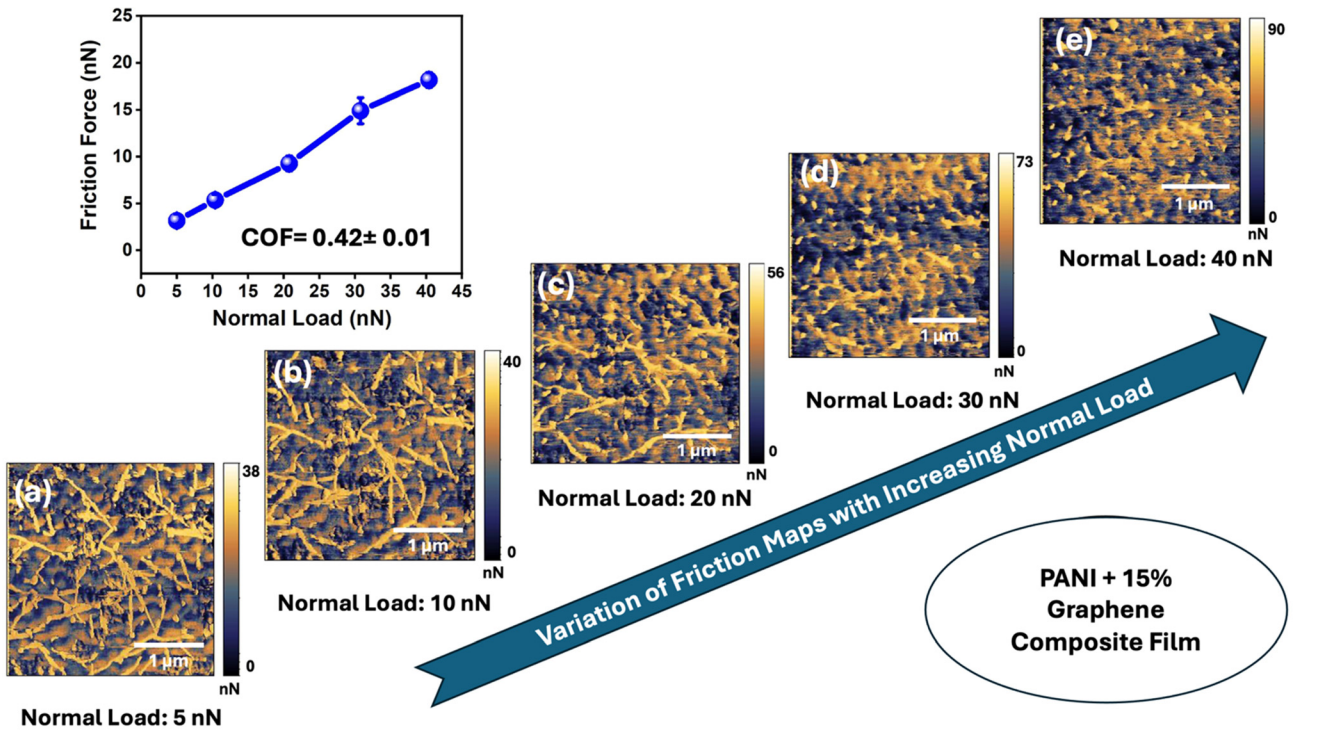

Fig. 5 Variation of friction maps (captured during the forward movement of the cantilever/trace motion) of the 15% graphene composite thin film with increasing normal loads. The friction maps at normal loads of (a) 5 nN, (b) 10 nN, (c) 20 nN, (d) 30 nN, and (e) 40 nN respectively. Inset image: plot of friction force *versus* normal load for the same thin film.

became negligible at the normal load of 40 nN. The same trend was observed in the 35% graphene composite thin film shown in Fig. S12.† In contrast to the 35% and 15% composite thin films, the removal of graphene patches with increasing normal loads was negligible for the 10% and 5% graphene composite thin films (Fig. S13 and S14†). For both the 10% and 5% graphene composite films, there was no significant difference in the concentration of graphene patches in between the lateral force maps at the applied normal loads of 5 nN and 40 nN. When the graphene was wearing out rapidly, the rate of increasing friction force gradually enhanced from the 5% graphene composite film to the 35% graphene composite thin films. Therefore, the possible reason for increasing the COF from the 5% to 35% film was the speedy removal of graphene with increasing normal load. It corroborated why the slope of the linear friction force *versus* the normal load curve increased gradually from the 5% graphene composite film to the 35% graphene composite film and reached the maximum for the pure PANI thin film due to the complete absence of a graphene filler material.

Conclusion

This research presents a new approach for fabricating optically transparent thin films of PANI–graphene nanocomposites using a solvent-free thermal evaporation technique with precise control over film thickness. The results reveal how the surface morphology and tribological properties of ultrathin polymer–graphene nanocomposite films can be tuned by varying the graphene content. Optical clarity was maintained across the different compositions, allowing detailed analysis of surface properties without visual interference. AFM provided valuable insights into how graphene dispersion affects the surface texture. The contact angle measurements demonstrated changes in wettability with different graphene concentrations.

The lateral force maps and friction loops revealed that graphene reduces friction force, with the effect being more pronounced in films with lower graphene contents. This reduction in friction was attributed to graphene's lubricating properties, which were more effective when graphene was well dispersed on the surface of the film. This study highlights the crucial role of graphene concentration and dispersion in enhancing the performance of polymer–graphene nanocomposite films. Precisely controlling the graphene content in the final film is essential for achieving optimal tribological properties. The results provide a deeper understanding of how to tailor the film properties for specific applications by controlling the graphene content and distribution, paving the way for advanced materials with enhanced functionality and performance. This approach can be extended to the tribological applications of other polymeric materials with graphene composites. In addition, graphene can be replaced with graphene oxide, carbon nanotubes, transition metal dichalcogenides, *etc*.

Data availability

The data supporting this article have been included as part of the ESI.†

Conflicts of interest

There are no conflicts to declare.

Acknowledgements

The authors acknowledge the use of characterization facilities at the Central Research Facility (CRF) and the Nanoscale Research Facility (NRF) at the Indian Institute of Technology (IIT) Delhi. NR acknowledges funding from DST-SERB through a Start-up Research Grant (SRG/2019/001143).

References

1 C. Harito, D. V. Bavykin, B. Yuliarto, H. K. Dipojono and F. C. Walsh, Polymer nanocomposites having a high filler content: synthesis, structures, properties, and applications, *Nanoscale*, 2019, **11**, 4653–4682.
2 Y.-T. Lin, T.-M. Don, C.-J. Wong, F.-C. Meng, Y.-J. Lin, S.-Y. Lee, C.-F. Lee and W.-Y. Chiu, Improvement of mechanical properties and anticorrosion performance of epoxy coatings by the introduction of polyaniline/graphene composite, *Surf. Coat. Technol.*, 2019, **374**, 1128–1138.
3 T. Lalire, C. Longuet and A. Taguet, Electrical properties of graphene/multiphase polymer nanocomposites: A review, *Carbon*, 2024, 119055.
4 M. O. Ansari, S. K. Yadav, J. W. Cho and F. Mohammad, Thermal stability in terms of DC electrical conductivity retention and the efficacy of mixing technique in the preparation of nanocomposites of graphene/polyaniline over the carbon nanotubes/polyaniline, *Composites, Part B*, 2013, **47**, 155–161.
5 C. Lee, X. Wei, J. W. Kysar and J. Hone, Measurement of the elastic properties and intrinsic strength of monolayer graphene, *science*, 2008, **321**, 385–388.
6 A. A. Balandin, S. Ghosh, W. Bao, I. Calizo, D. Teweldebrhan, F. Miao and C. N. Lau, Superior thermal conductivity of single-layer graphene, *Nano Lett.*, 2008, **8**, 902–907.
7 K. S. Novoselov, A. K. Geim, S. V. Morozov, D.-E. Jiang, Y. Zhang, S. V. Dubonos, I. V. Grigorieva and A. A. Firsov, Electric field effect in atomically thin carbon films, *Science*, 2004, **306**, 666–669.
8 D. Berman, A. Erdemir and A. V. Sumant, Graphene: a new emerging lubricant, *Mater. Today*, 2014, **17**, 31–42.
9 A. G. MacDiarmid and A. J. Epstein, Polyanilines: a novel class of conducting polymers, *Faraday Discuss. Chem. Soc.*, 1989, **88**, 317–332.

10 Y. K. Choi, H. J. Kim, S. R. Kim, Y. M. Cho and D. J. Ahn, Enhanced thermal stability of polyaniline with polymerizable dopants, *Macromolecules*, 2017, **50**, 3164–3170.
11 Y. Wang and K. Levon, *Macromolecular symposia*, 2012, pp. 240–247.
12 H. Wang, Q. Hao, X. Yang, L. Lu and X. Wang, A nanostructured graphene/polyaniline hybrid material for supercapacitors, *Nanoscale*, 2010, **2**, 2164–2170.
13 R. Lenin, A. Singh and C. Bera, Effect of dopants and morphology on the electrical properties of polyaniline for various applications, *J. Mater. Sci.: Mater. Electron.*, 2021, **32**, 24710–24725.
14 R. V. Ingle, S. F. Shaikh, P. K. Bhujbal, H. M. Pathan and V. A. Tabhane, Polyaniline doped with protonic acids: optical and morphological studies, *ES Mater. Manuf.*, 2020, **8**, 54–59.
15 E. Coşkun, E. A. Zaragoza-Contreras and H. J. Salavagione, Synthesis of sulfonated graphene/polyaniline composites with improved electroactivity, *Carbon*, 2012, **50**, 2235–2243.
16 N. A. Kumar, H.-J. Choi, Y. R. Shin, D. W. Chang, L. Dai and J.-B. Baek, Polyaniline-grafted reduced graphene oxide for efficient electrochemical supercapacitors, *ACS Nano*, 2012, **6**, 1715–1723.
17 J. Lu, W. Liu, H. Ling, J. Kong, G. Ding, D. Zhou and X. Lu, Layer-by-layer assembled sulfonated-graphene/polyaniline nanocomposite films: enhanced electrical and ionic conductivities, and electrochromic properties, *RSC Adv.*, 2012, **2**, 10537–10543.
18 Z. Wang, Q. E. Zhang, S. Long, Y. Luo, P. Yu, Z. Tan, J. Bai, B. Qu, Y. Yang, J. Shi, *et al.*, Three-dimensional printing of polyaniline/reduced graphene oxide composite for high-performance planar supercapacitor, *ACS Appl. Mater. Interfaces*, 2018, **10**, 10437–10444.
19 F. Balqis, B. Prakoso, N. Hanif Hawari, C. Eldona and A. Sumboja, Recent development of polyaniline/graphene composite electrodes for flexible supercapacitor devices, *ChemNanoMat*, 2022, **8**, e202200151.
20 D. Gui, C. Liu, F. Chen and J. Liu, Preparation of polyaniline/graphene oxide nanocomposite for the application of supercapacitor, *Appl. Surf. Sci.*, 2014, **307**, 172–177.
21 V. C. Valsalakumar, A. S. Joseph, J. Piyus and S. Vasudevan, Polyaniline–graphene oxide composites decorated with ZrO2 nanoparticles for use in screen-printed electrodes for real-time l-tyrosine sensing, *ACS Appl. Nano Mater.*, 2023, **6**, 8382–8395.
22 A. Al-Hamry, T. Lu, J. Bai, A. Adiraju, T. K. Ega, L. Paterno, I. A. Pašti and O. Kanoun, Versatile sensing capabilities of layer-by-layer deposited polyaniline-reduced graphene oxide composite-based sensors, *Sens. Actuators, B*, 2023, **390**, 133988.
23 Z. Zhao, C. Ma, L. Xu, Z. Yu, D. Wang, L. Jiang, X. Jiang and G. Gao, Conductive Polyaniline-Based Microwire Arrays for SO2 Gas Detection, *ACS Appl. Mater. Interfaces*, 2023, **15**, 38938–38945.
24 M. Jamdegni and A. Kaur, Electrochromic behavior of highly stable, flexible electrochromic electrode based on covalently bonded polyaniline-graphene quantum dot composite, *J. Electrochem. Soc.*, 2019, **166**, H502.
25 H. Gong, J. Ai, W. Li, J. Zhu, Q. Zhang, J. Liu, Y. Jin and H. Wang, Self-driven infrared electrochromic device with tunable optical and thermal management, *ACS Appl. Mater. Interfaces*, 2021, **13**, 50319–50328.
26 R. Maurya, A. R. Siddiqui, P. K. Katiyar and K. Balani, Mechanical, tribological and anti-corrosive properties of polyaniline/graphene coated Mg-9Li-7Al-1Sn and Mg-9Li-5Al-3Sn-1Zn alloys, *J. Mater. Sci. Technol.*, 2019, **35**, 1767–1778.
27 L. Liu, W. Zhou, Y. Chen, S. Jiao and P. Huang, Pressure-assisted synthesis of a polyaniline–graphite oxide (PANI–GO) hybrid and its friction reducing behavior in liquid paraffin (LP), *New J. Chem.*, 2018, **42**, 936–942.
28 D. K. Verma, S. Prajapati, M. Sahu, S. Singh, B. Kumar, A. K. Singh, N. Shukla, Kavita and R. B. Rastogi, Superlubricity of Nanocomposites of Polyaniline-Functionalized Reduced Graphene Oxide with Yttrium and Vanadium-Codoped Zinc Oxide Nanoparticles, *ACS Appl. Eng. Mater.*, 2024, **2**, 156–169.
29 Z. Cao and Y. Xia, Synthesis and tribological properties of polyaniline functionalized by ionic liquids, *J. Mater. Sci.*, 2018, **53**, 7060–7071.
30 Y. Xia, Y. Wang, C. Hu and X. Feng, Conductivity and tribological properties of IL-PANI/WS2 composite material in lithium complex grease, *Friction*, 2023, **11**, 977–991.
31 A. K. Singh, N. Shukla, D. K. Verma, B. Kumar, S. Singh, R. B. Rastogi, *et al.*, Polyaniline intercalated vanadium pentoxide nanosheets for the improvement of lubricity of base oil, *Colloids Surf., A*, 2022, **642**, 128644.
32 Z. Lin, X. Jia, Y. Li, H. Song and J. Yang, Improved mechanical/tribological properties of polyimide/carbon fabric composites by in situ-grown polyaniline nanofibers, *Mater. Chem. Phys.*, 2021, **258**, 123972.
33 C. P. Green, H. Lioe, J. P. Cleveland, R. Proksch, P. Mulvaney and J. E. Sader, Normal and torsional spring constants of atomic force microscope cantilevers, *Rev. Sci. Instrum.*, 2004, **75**, 1988–1996.
34 J. E. Sader, I. Larson, P. Mulvaney and L. R. White, Method for the calibration of atomic force microscope cantilevers, *Rev. Sci. Instrum.*, 1995, **66**, 3789–3798.
35 U. Schwarz, P. Köster and R. Wiesendanger, Quantitative analysis of lateral force microscopy experiments, *Rev. Sci. Instrum.*, 1996, **67**, 2560–2567.
36 X. Feng, S. Kwon, J. Y. Park and M. Salmeron, Superlubric sliding of graphene nanoflakes on graphene, *ACS Nano*, 2013, **7**, 1718–1724.
37 K.-S. Kim, H.-J. Lee, C. Lee, S.-K. Lee, H. Jang, J.-H. Ahn, J.-H. Kim and H.-J. Lee, Chemical vapor deposition-grown graphene: the thinnest solid lubricant, *ACS Nano*, 2011, **5**, 5107–5114.
38 S. Kawai, A. Benassi, E. Gnecco, H. Söde, R. Pawlak, X. Feng, K. Müllen, D. Passerone, C. A. Pignedoli, P. Ruffieux, *et al.*, Superlubricity of graphene nanoribbons on gold surfaces, *Science*, 2016, **351**, 957–961.

39 P. Wu, X. Li, C. Zhang, X. Chen, S. Lin, H. Sun, C.-T. Lin, H. Zhu and J. Luo, Self-assembled graphene film as low friction solid lubricant in macroscale contact, *ACS Appl. Mater. Interfaces*, 2017, **9**, 21554–21562.
40 T. Filleter, J. L. McChesney, A. Bostwick, E. Rotenberg, K. V. Emtsev, T. Seyller, K. Horn and R. Bennewitz, Friction and dissipation in epitaxial graphene films, *Phys. Rev. Lett.*, 2009, **102**, 086102.
41 M. Dienwiebel, G. S. Verhoeven, N. Pradeep, J. W. Frenken, J. A. Heimberg and H. W. Zandbergen, Superlubricity of graphite, *Phys. Rev. Lett.*, 2004, **92**, 126101.